Research Article

Numerical Simulation of CAARC Standard High-Rise Building Model Based on MRT-LBM Large Eddy Simulation

Rui Zhao,[1,2] Zehua Feng [ID],[1] Danhui Dan,[1,3] Yuhang Wu [ID],[1] and Xianduo Li[1]

[1]*School of Civil Engineering and Architecture, Xinjiang University, Urumqi 830047, China*
[2]*Xin Jiang Key Lab of Building Structure and Earthquake Resistance, Urumqi 830047, China*
[3]*Department of Bridge Engineering, Tongji University, Shangha 200082, China*

Correspondence should be addressed to Zehua Feng; fengzehua@stu.xju.edu.cn

The calculation of wind load of high-rise buildings depends on the wind pressure distribution data and wind pressure coefficient on the outer surface of the building, but the actual wind pressure measurement of high-rise buildings is difficult to carry out. In order to obtain the effective wind pressure coefficient of the building and the application of the extended lattice Boltzmann method (LBM) in the wind resistance of high-rise buildings, in this paper, the wall-adapting local eddy (WALE) model, dynamic Smagorinsky model (DSM), and Smagorinsky model (SM) are embedded into LBM with multiple-relaxation-time (MRT) format. Three LBM large eddy simulation models, MRT-LBM-WALE, MRT-LBM-DSM, and MRT-LBM-SM, which can simulate the flow around a bluff body with high Rayleigh number, are constructed by using the subgrid eddy viscosity to modify the kinematic viscosity of LBM. Finally, the three turbulence models are used to simulate and analyze the three-dimensional steady wind flow field of a single high-rise building of the standard CAARC high-rise building model in the atmospheric boundary layer, and the numerical results are analyzed and compared with the wind tunnel test results. The results show that the numerical simulation better reflects the flow characteristics and surface wind pressure of the wind environment around the high-rise building. On the windward side, it fits well with the test results. On the crosswind side and leeward side, the numerical simulation results are between the NPL and TJ-2 test results. The windward side is subject to positive pressure, which is the highest at 2/3 of the height of the windward side and low on both sides and below. The leeward and crosswind surfaces of the building are all under negative pressure. The simulation results of the three turbulence models have little difference, which provides a basis for the study of the flow around the bluff body of high-rise buildings. It is proved that the numerical solutions of the three models are in good agreement with the experimental solutions, and the real subgrid eddy viscosity near the wall can be obtained, which can accurately predict the development of turbulent flow.

1. Introduction

One of the main purposes of studying the air flow around high-rise buildings under the action of wind is to study the wind pressure distribution law of wind load on the outer surface of high-rise buildings. At present, there are three traditional research methods: field measurement, wind tunnel test [1, 2], and numerical simulation method based on computational fluid dynamics (CFD) [3, 4]. However, the actual wind pressure measurement of high-rise buildings is difficult to carry out. The wind tunnel test is only suitable for specific structures, and there are some problems, such as high cost and long test cycle. The numerical simulation method not only has the ability to simulate real and ideal conditions, but also has the advantages of less cost and short time. It can completely measure the required wind pressure and wind speed in real time and realize the visualization of calculation results. Therefore, the numerical simulation method based on computational fluid dynamics has gradually become an important method to predict the surface wind pressure, surrounding wind speed, and turbulence characteristics of buildings.

At present, Reynolds-averaged Navier–Stokes (RANS) [5] and large eddy simulation (LES) [6] are often used as CFD numerical methods for wind pressure distribution on the outer surface of buildings. Therefore, the accuracy of its simulation has become the focus of scholars at home and abroad. In order to fully illustrate the accuracy of the model, scholars often compare the wind tunnel test results of the standard model of high-rise buildings with the CFD numerical results. In foreign countries, for example, Huang et al. [7] used the large eddy simulation method, Reynolds time average method, and wind tunnel test to compare the results of surface wind pressure and overall wind force on the windward surface of the CAARC model. The results show that the simulation results of the LES method in building overall resistance and crosswind fluctuating lift are better than the RANS method. The numerical results of average wind pressure calculated by Braun and Awruch [8] using the LES method fit well with the results obtained by different wind tunnel test institutions. The results show that the wind speed profile affects the average wind pressure on the building surface. Daniels et al. [9]. pointed out that the numerical results of fluctuating wind pressure on building crosswind simulated by the LES method are quite different from the experimental results; the RANS method fails to capture the separation bubble at the corner of the building, which will lead to the wind suction at the side edge. Elshaer et al. [10] studied the average wind pressure at the windward height of 2/3 of the CAARC model and showed that the stagnation point height of LES was greater than the test results because the LES method captured some low-frequency pulsating components missing in the test incoming flow due to the limitation of laboratory cross section. In China, Nie et al. [11] used the RANS method to simulate the surface wind pressure at the height of 2/3 of the windward surface, crosswind surface, and leeward surface of the CAARC standard model. The results show that the numerical results of the wind pressure on the windward surface simulated by the RANS method are less different from the test results, but the wind pressure on the crosswind surface is more different from the test results. This is because the RANS method can only give the average motion results of the complex motion with high Rayleigh number and cannot reflect the details of the flow field disorder, while the side flow is in the separation zone. Therefore, there are some differences between the experimental results and the numerical results. In conclusion, the LES method is more accurate than the RANS method in simulating the surface wind pressure of the CAARC model.

In recent years, a new CFD method has been applied in many fields because it can explicitly solve the pressure equation, is easy to parallel, and has the advantages of high precision [12–16]. The air turbulence of the CAARC standard model is a typical high Rayleigh number flow. If only theoretically, LBM can directly simulate turbulence, but due to the limitation of current calculation conditions, it is easy to lead to instability. In order to calculate turbulence, it is usually necessary to embed the turbulence model of the RANS method or the subgrid eddy viscosity model of the LES method into LBM. Yu et al. [17]

took the grid scale of LBM as the filtering scale and embedded the Smagorinsky subgrid eddy viscosity model into LBM. The result is simple and has high accuracy [18]. However, for the simulation of near wall flow, the Smagorinsky model has some defects. In fact, due to the proximity to the wall, the velocity decreases, the near wall flow gradually turns into laminar flow, and the subgrid eddy viscosity on the wall should be equal to zero. The subgrid eddy viscosity obtained by the Smagorinsky eddy viscosity model is not zero, which is inconsistent with the reality. The dynamic Smagorinsky model proposed by Lilly [19] and Germano et al. [20] improves the Smagorinsky model. This model can give the correct asymptotic relationship on the solid wall, but if the model coefficient becomes negative, there will be numerical instability sometimes. The WALE viscosity model [21–24] can obtain the ideal subgrid eddy viscosity distribution without applying the wall function or adjusting the model constant near the wall, which can well predict the flow near the wall. Therefore, in this paper, the subgrid eddy viscosity model, wall-adapting local eddy (WALE) model, dynamic Smagorinsky model, and Smagorinsky model are embedded into the LBM with multiple-relaxation-time format. Three LBM large eddy simulation models, mrt-lbm-wale, mrt-lbm-dsm, and mrt-lbm-sm, which can simulate the flow around a bluff body with high Rayleigh number, are constructed by using the subgrid eddy viscosity to modify the kinematic viscosity of LBM. Finally, the three turbulence models are used to simulate and analyze the three-dimensional steady wind flow field of a single high-rise building with the atmospheric boundary layer CAARC standard model, and the numerical results are compared with the wind tunnel test results.

2. MRT-LBM Large Eddy Simulation

2.1. MRT-LBM Evolution Equation. The classic D3Q19 model is shown in Figure 1.

The discrete speed is

$$
e_i = \begin{bmatrix} 0 & 1 & -1 & 0 & 0 & 0 & 0 & 1 & -1 & 1 & -1 & 1 & -1 & -1 & 1 & 0 & 0 & 0 & 0 \\ 0 & 0 & 0 & 1 & -1 & 0 & 0 & 1 & -1 & -1 & 1 & 0 & 0 & 0 & 0 & 1 & -1 & 1 & -1 \\ 0 & 0 & 0 & 0 & 0 & 1 & -1 & 0 & 0 & 0 & 0 & 1 & -1 & 1 & -1 & 1 & -1 & -1 & 1 \end{bmatrix},
$$

(1)

where $C = 1$, and the evolution equation of multiple relaxation LBM is [25–27]

$$
f(x + e_i \delta_t, t + \delta_t) = f(x, t) - M^{-1}[m - m^{eq}], \quad (2)
$$

where x is the spatial position; e_i is the molecular discrete velocity vector; t is the time; f represents the distribution function on the lattice node; m is the moment, m^{eq} represents the moment equilibrium state; M represents an orthogonal transformation matrix, and

$$
m = Mf, \quad f = M^{-1}m. \quad (3)
$$

Macroparameters ρ (density), p (pressure), and velocity $u = (u_x, u_y)$ can be obtained by solving the moment of distribution function F. Here $\rho = \rho_0 + \delta\rho$, among $\rho_0 = 1$,
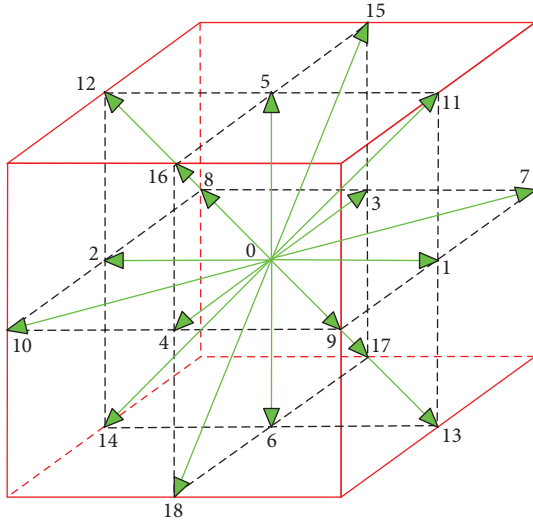
FIGURE 1: D3Q19 model of 19 velocities in 3-D.

$\delta\rho = \Sigma f_i$, $\rho u = \Sigma f_i e_i$, and $p = \delta\rho c_s^2$, C_s represents the speed of sound, and $C_s = 1/\sqrt{3}$, $M =$

$$\begin{bmatrix}
1 & 1 & 1 & 1 & 1 & 1 & 1 & 1 & 1 & 1 & 1 & 1 & 1 & 1 & 1 & 1 & 1 & 1 & 1 \\
-30 & -11 & -11 & -11 & -11 & -11 & -11 & 8 & 8 & 8 & 8 & 8 & 8 & 8 & 8 & 8 & 8 & 8 & 8 \\
12 & -4 & -4 & -4 & -4 & -4 & -4 & 1 & 1 & 1 & 1 & 1 & 1 & 1 & 1 & 1 & 1 & 1 & 1 \\
0 & 1 & -1 & 0 & 0 & 0 & 0 & 1 & -1 & 1 & -1 & 0 & 0 & 1 & -1 & 1 & -1 & 0 & 0 \\
0 & -4 & 4 & 0 & 0 & 0 & 0 & 1 & -1 & 1 & -1 & 0 & 0 & 1 & -1 & 1 & -1 & 0 & 0 \\
0 & 0 & 0 & 1 & -1 & 0 & 0 & 1 & -1 & 0 & 0 & 0 & 0 & -1 & -1 & 1 & 0 & 1 & -1 \\
0 & 0 & 0 & -4 & 4 & 0 & 0 & 1 & -1 & 0 & 0 & 0 & 0 & -1 & -1 & 1 & 0 & 1 & -1 \\
0 & 0 & 0 & 0 & 0 & 1 & -1 & 0 & 0 & 1 & -1 & 1 & -1 & 0 & 0 & -1 & 1 & -1 & 1 \\
0 & 0 & 0 & 0 & 0 & -4 & 4 & 0 & 0 & 1 & -1 & 1 & -1 & 0 & 0 & -1 & 1 & -1 & 1 \\
0 & 2 & 2 & -1 & -1 & -1 & -1 & 1 & 1 & 1 & 1 & -2 & -2 & 1 & 1 & 1 & 1 & -2 & -2 \\
0 & -4 & -4 & 2 & 2 & 2 & 2 & 1 & 1 & 1 & 1 & -2 & -2 & 1 & 1 & 1 & 1 & -2 & -2 \\
0 & 0 & 0 & 1 & 1 & -1 & -1 & 1 & 1 & -1 & -1 & 0 & 0 & 1 & 1 & -1 & -1 & 0 & 0 \\
0 & 0 & 0 & -2 & -2 & 2 & 2 & 1 & 1 & -1 & -1 & 0 & 0 & 1 & 1 & -1 & -1 & 0 & 0 \\
0 & 0 & 0 & 0 & 0 & 0 & 0 & 1 & 1 & 0 & 0 & 0 & 0 & -1 & -1 & 0 & 0 & 0 & 0 \\
0 & 0 & 0 & 0 & 0 & 0 & 0 & 0 & 0 & 0 & 0 & 1 & 1 & 0 & 0 & 0 & 0 & -1 & -1 \\
0 & 0 & 0 & 0 & 0 & 0 & 0 & 0 & 0 & 1 & 1 & 0 & 0 & 0 & 0 & -1 & -1 & 0 & 0 \\
0 & 0 & 0 & 0 & 0 & 0 & 0 & 1 & -1 & -1 & 1 & 0 & 0 & 1 & -1 & -1 & 1 & 0 & 0 \\
0 & 0 & 0 & 0 & 0 & 0 & 0 & -1 & 1 & 0 & 0 & 1 & -1 & 1 & -1 & 0 & 0 & 1 & -1 \\
0 & 0 & 0 & 0 & 0 & 0 & 0 & 0 & 0 & 1 & -1 & -1 & 1 & 0 & 0 & -1 & 1 & 1 & -1
\end{bmatrix}$$

In the classical D3Q19 model, the elements in the moment are

$$m = \begin{bmatrix} \rho e \varepsilon j_x q_x j_y q_y j_z q_z 3 p_{xx} 3\pi_{xx} p_{ww} p_{xy} p_{yz} p_{zx} t_x t_y t_z \end{bmatrix}^T, \quad (4)$$

where $j_x = \rho u_x$, $j_y = \rho u_y$, and $j_z = \rho u_z$.

The equilibrium state is

$$m^{eq} = \rho \begin{pmatrix} 1, -11 + 19u^2, \alpha + \beta u^2, u_x, -\dfrac{2}{3}u_x, u_y, -\dfrac{2}{3}u_y, u_z, \\[2mm] -\dfrac{2}{3}u_z, 3u_x^2 - u^2, u_y^2 - u_x^2, u_x u_y, u_y u_z, u_z u_x, \dfrac{\gamma p_{xx}^{eq}}{\rho}, \dfrac{\gamma p_{ww}^{eq}}{\rho}, 0, 0, 0 \end{pmatrix}, \quad (5)$$

where $u^2 = u_x^2 - u_y^2$, and the distribution function expression of equilibrium state is

$$f_i^{eq} = w_i \left\{ \delta\rho + \rho_0 \left[\dfrac{e_i u}{c_s^2} + \dfrac{(e_i u)^2}{2c_s^4} - \dfrac{uu}{2c_s^2} \right] \right\}. \quad (6)$$

The weighting coefficient w_i is taken as the value:

$$w_0 = \dfrac{1}{3},$$

$$w_i = \dfrac{1}{18} \ (i = 1, 2, 3, 4, 5, 6), \quad (7)$$

$$w_i = \dfrac{1}{36} \ (i = 7, 8, 9, 10, \ldots, 18).$$

Relaxation matrix S is as follows:

$$S = \text{diag} \begin{bmatrix} 0 S_e S_\varepsilon 0 S_q 0 S_q 0 S_q 0 S_v S_\pi S_v S_\pi S_v S_v S_v S_t S_t S_t \end{bmatrix}. \quad (8)$$

In the multiple relaxation model, the shear and volume viscosities are

$$v = \dfrac{1}{3}\left(\dfrac{1}{S_V} - \dfrac{1}{2}\right)\delta t,$$

$$\varepsilon = \dfrac{2}{9}\left(\dfrac{1}{S_e} - \dfrac{1}{2}\right)\delta t. \quad (9)$$

In: relaxation parameters S_V is shear viscosity, S_e is volume viscosity, and S_q and S_ε represents free parameters.

2.2. Realization Method of MRT-LBM-LES Large Eddy Simulation.

In LES, the subgrid vortices are viscous:

$$v_t = (C_s\Delta)^2 w, \quad (10)$$

where w is the LES operator and C_s as the LES model constant. In this paper, the constant value of wale model C_s is 0.2 because the constant value of the wale model is usually 0.2. The Smagorinsky constant value is usually in the curve of 0.1-0.2. In this paper, C_s of SM and DSM is taken as 0.12. Δ is a filter function.

In the Smagorinsky model, $w = \sqrt{2\overline{S}_{ij}\overline{S}_{ij}}$, $\overline{S}_{ij} = 1/2$ $(\partial\overline{v}_i/\partial\overline{x}_j + \partial\overline{v}_j/\partial\overline{x}_i)$, the dynamic Smagorinsky model is a modification of the Smagorinsky model, where C_s is dynamically calculated according to the decomposed motion scale information. Therefore, it may change in time and space, and the solution method refers to [14]. The WALE model is affected by the effects of both the rotation rate tensor and the strain rate tensor on V_t, [21]

$$w = \dfrac{\left(G_{ij}^d G_{ij}^d\right)^{3/2}}{\left(S_{ij}S_{ij}\right)^{5/2} + \left(G_{ij}^d G_{ij}^d\right)^{5/4}},$$

$$\overline{\Omega}_{ij} = \dfrac{1}{2}\left(\dfrac{\partial\overline{v}_i}{\partial\overline{x}_j} - \dfrac{\partial\overline{v}_j}{\partial\overline{x}_i}\right), \quad (11)$$

$$G_{ij}^d = \overline{S}_{ik}\overline{S}_{kj} + \overline{\Omega}_{ik}\overline{\Omega}_{kj} - \dfrac{1}{3}\delta_{ij}\left(\overline{S}_{ij}\overline{S}_{ij} - \overline{\Omega}_{ij}\overline{\Omega}_{ij}\right),$$

where it is required to solve the subgrid eddy viscosity of wale viscosity model and only need to solve $\overline{\Omega}_{ij}$ and $\overline{S}_{ij}$. $\overline{\Omega}_{\alpha\beta}$ The Cartesian node of LBM can be used as the difference

node, and then calculated by the finite difference method, $\overline{S}_{ij}$ can use the nonequilibrium moment f_k^{eq} solution:

$$\overline{S}_{ij} = \sum_k^{18} c_{ki} c_{kj} f_k^{eq}, \quad f_k^{eq} = M^{-1} \left(M f - m^{eq} \right). \tag{12}$$

Consider ν_t after t, and the total V_{all} of MRT-LBM is taken

$$V_{\text{all}} = \nu_0 + \nu_t, \tag{13}$$

where V_{all} is the total effective kinematic viscosity coefficient, ν_0 is the kinematic viscosity coefficient, equal to UL/Re; U fetch flow velocity; L is the characteristic length; and Re is the Rayleigh number.

In the evolution equation of MRT-LBM, MRT-LBM large eddy simulation is realized by updating the relaxation coefficient of the relaxation matrix by using the effective motion viscosity coefficient. In addition, the subgrid scale model adopts WALE, DSM, and SM eddy viscosity models, so the model can be called MRT-LBM-WALE and MRT-LBM-DSM.

3. Numerical Study

3.1. Geometric Modeling and Meshing. The CAARC standard model is a standard high-rise building model proposed at the Federal Aviation Advisory Committee in 1969, which is used to test the wind tunnel test results of various high-rise building models simulating natural wind. In recent years, domestic and foreign scholars have also checked the CFD simulation results based on this model [10, 11]. The geometric dimension of the CAARC standard die is 30.48 $(D_x) \times 45.72$ $(D_y) \times 182.88$ (H) m³, and 20 pressure measuring points are evenly arranged on the 2/3H height horizontal plane of the model. See Figure 2 for the geometric dimensions of the model, the arrangement of surface pressure measuring points, and the inflow direction.

In this paper, the CAARC standard model is analyzed by full-scale modeling, and the calculated watershed is 1800 m × 600 m × 1000 m, the buildings are placed 1/3 forward along the river basin, and the blocking rate of the river basin meets the requirements of less than 3%. The geometric dimensions of the model and the layout of pressure measuring points are shown in Figure 2. The discretization of its spatial domain adopts adaptive grid division, that is, 0.5 m grid is used near the CAARC wall, 8 m grid is used far away from the wall, and the grids in the transition area of the two grids are 4 m, 2 m, and 1 m, respectively. The grid division of the computing domain is shown in Figure 3.

3.2. Setting of Boundary Conditions. The inflow conditions used in the numerical simulation are the same as those used in the wind tunnel test. The velocity inflow boundary condition simulates the exponential distribution of the wind speed profile in the atmospheric boundary layer, that is,

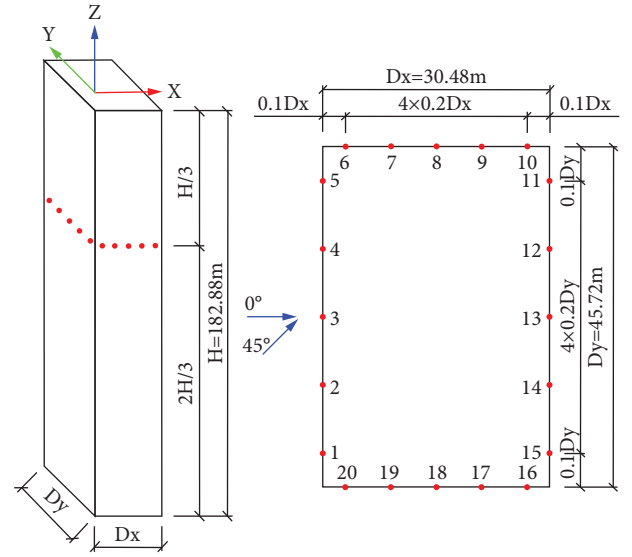$$U = U_0 \left(\frac{Z}{Z_0} \right)^{\alpha}, \tag{14}$$

FIGURE 2: Geometric dimensions of CAARC standard mould and layout of pressure measuring points.
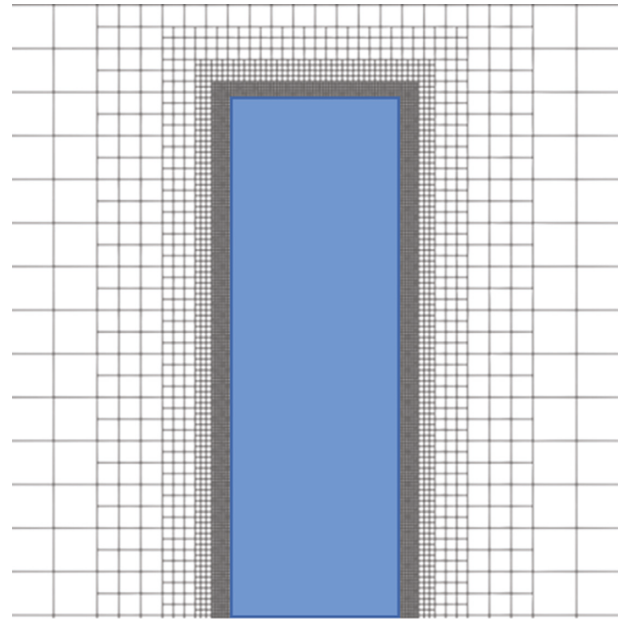

FIGURE 3: Grid division of the computing domain.

where Z_0 and U_0 are the wind speed at the reference height (top of the model) and the reference height, respectively. According to the wind tunnel test [11], the wind speed at the reference height (182.88 m) and the reference height of the building are taken, respectively, (the test wind speeds of class B and class D wind fields are 11.7 m/s and 12.7 m/s, respectively); Z, U is the height of a point in the basin and the average wind speed at that point; α is the ground roughness index. For class B and class D wind fields, 0.16 and 0.3 are taken, respectively [28].

Because the outflow is basically completely developed, the velocity outflow boundary condition adopts the fully developed outflow boundary condition (outflow) [29], and the gradient of any physical quantity of the flow field along
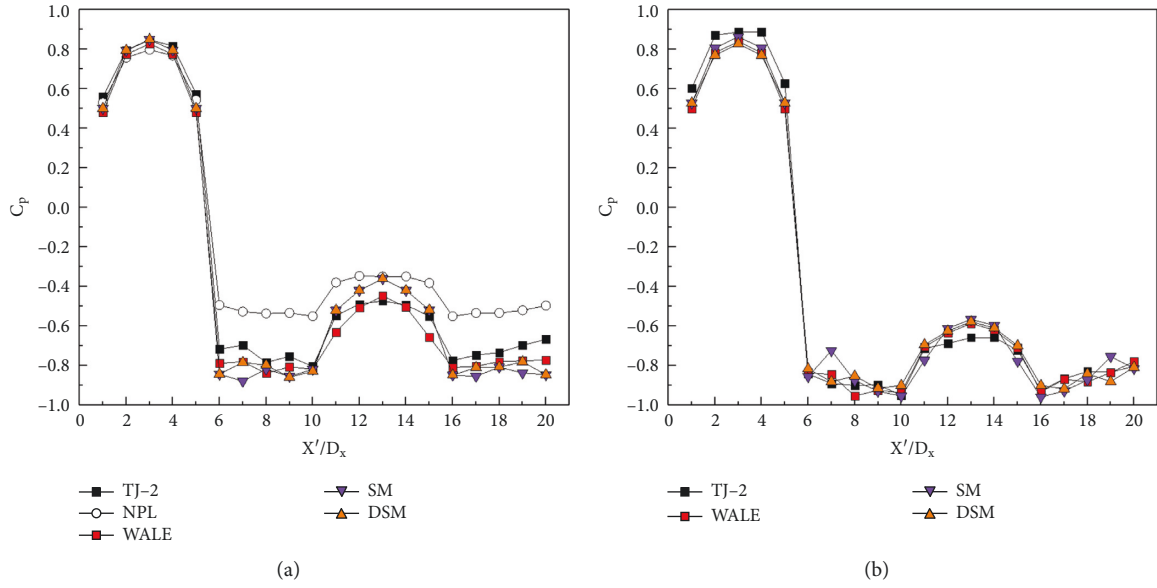
FIGURE 4: Average wind pressure coefficient at 0° wind direction angle. (a) Class D wind farm. (b) Class B wind farm.
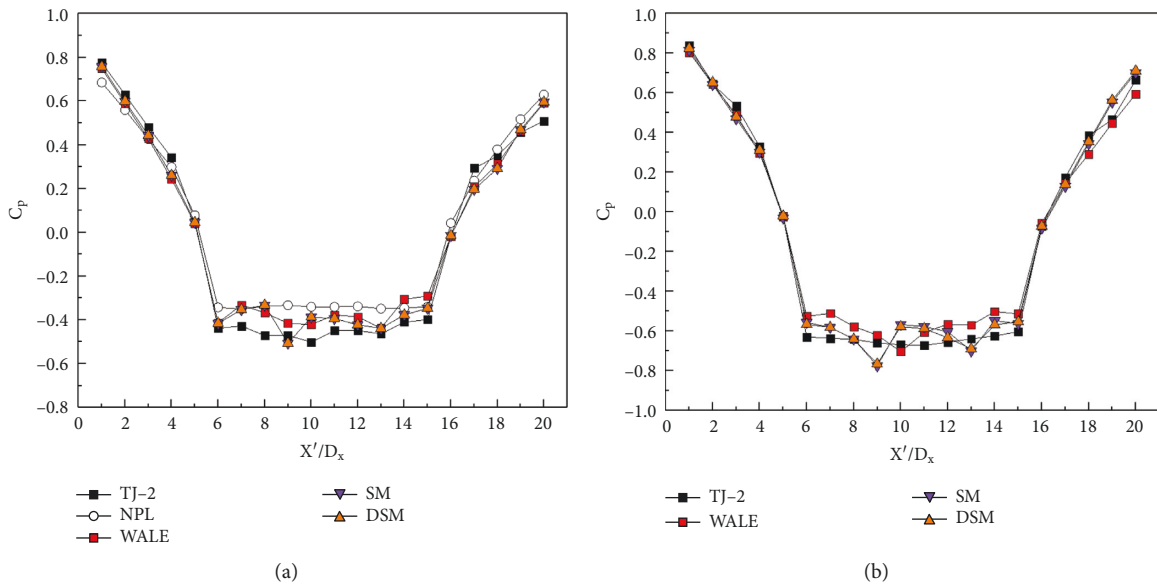

FIGURE 5: Average wind pressure coefficient at 45° wind direction angle. (a) Class D wind farm. (b) Class B wind farm.

the outlet normal direction is zero, that is, $\partial\phi/\partial n = 0$. Both sides and top sides of the basin adopt periodic boundary conditions, PBC, [30] and building surface and ground adopt (wall) [31] boundary conditions without sliding.

4. Calculation Results and Analysis

4.1. Distribution of Wind Pressure Coefficient at 2/3H Height. Using the large eddy simulation (LES) method of the LBM mentioned above, namely, MRT-LBM-WALE, MRT-LBM-DSM, and MRT-LBM-SM, three turbulence models are constructed to numerically simulate the wind field of CAARC standard model building, and the wind pressure

coefficients under two working conditions of 0° and 45° wind angle of class B and class D sites are calculated, respectively [32, 33].

In the CAARC standard model wind tunnel test, the dimensionless wind pressure coefficient C_p takes the flow pressure at the top height H of the scale model as the reference wind pressure; that is, the pressure coefficient is calculated by the following formula [34–44]:

$$C_P = \frac{2(P - P_0)}{\rho U_0^2},$$ (15)

where P is the average pressure of standard pressure measuring points, and the measuring points are shown in
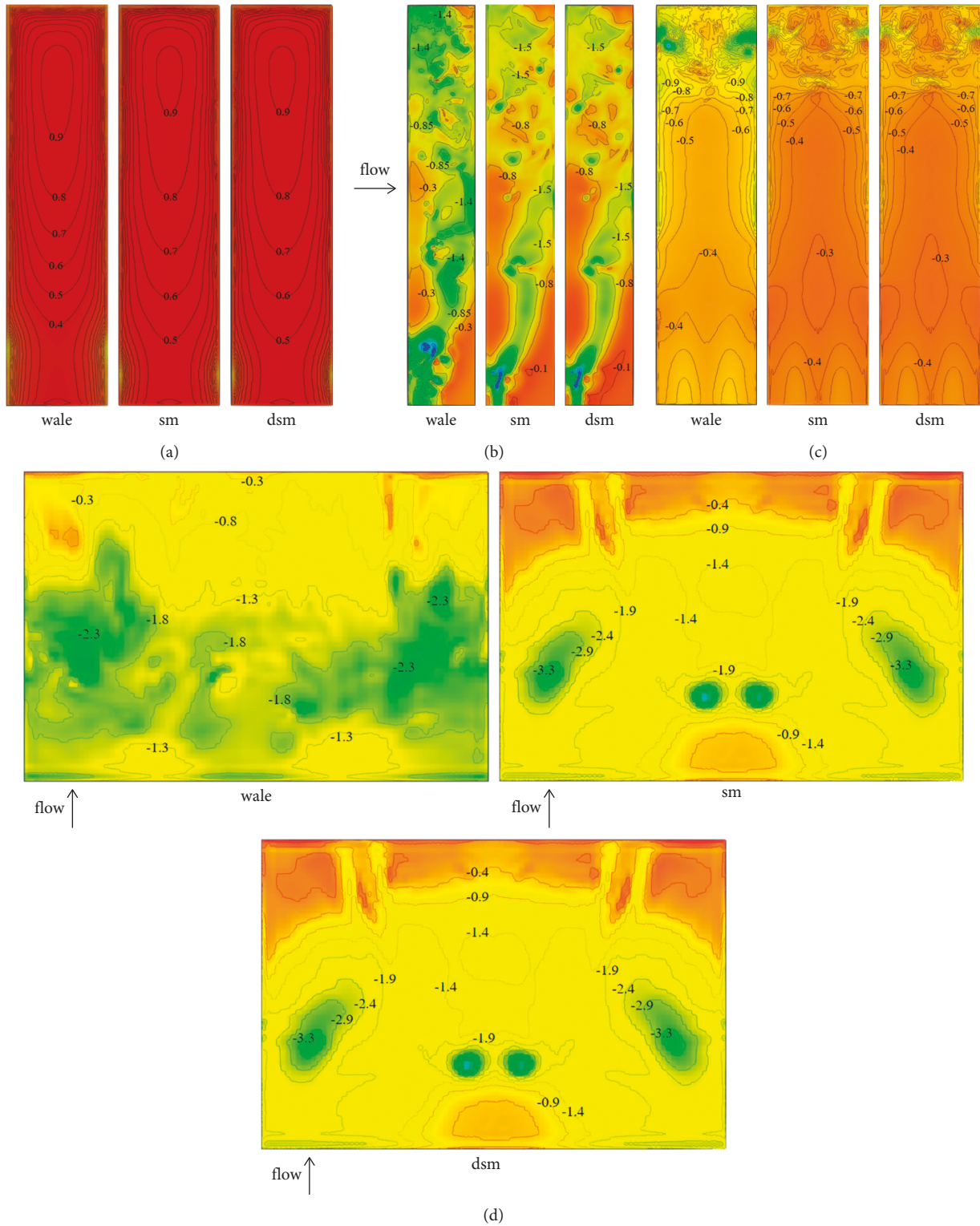
FIGURE 6: Calculation results of average wind pressure coefficient on the surface of class D wind field at 0° wind direction angle. (a) Windward side. (b) Crosswind surface. (c) Leeward side. (d) Top surface.

Figure 2; P_0 is the static pressure at the top height H; ρ is the air density, with the value of 1.225 kg/m^3; and U_0 is the wind speed at the top height H.

In this paper, the numerical calculation results of the pressure coefficient at the height of $2/3H$ (122 m) are compared with the test results of the NPL, National Physical
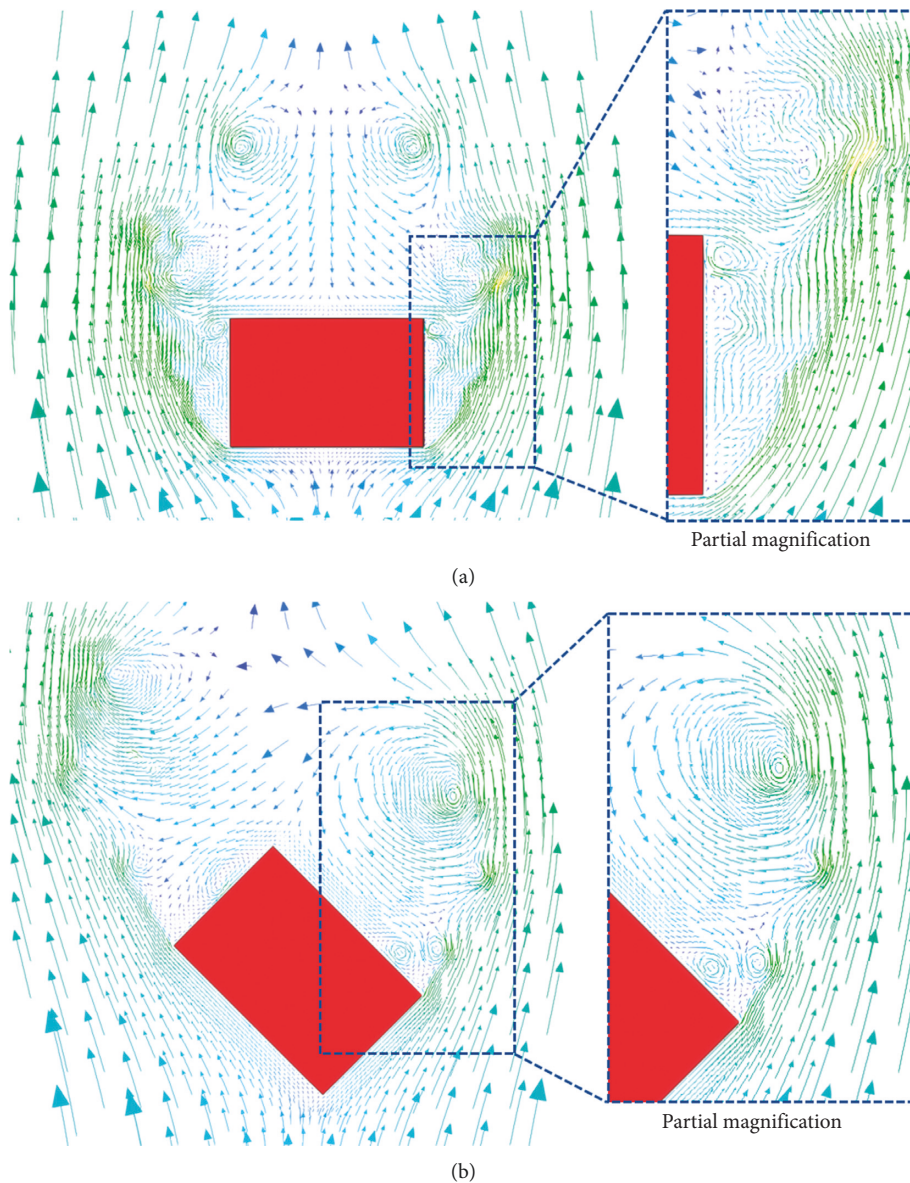
(a)

(b)

FIGURE 7: Velocity distribution at 2/3H height of the wale model of class D wind field. (a) 0° wind angle. (b) 45° wind angle.

Laboratory, and the TJ-2 wind tunnel test results of Tongji University [22] at the standard pressure measuring point. The numerical calculation results are shown in Figures 4 and 5.

It can be seen from Figures 4 and 5 that for the simulation study of the CAARC standard model, the numerical results of the three turbulence models are consistent with the test results, and the overall trend of the numerical results is in good agreement with the test results, which is closer to the test results of the TJ-2 wind tunnel of Tongji University. Among them, for the windward side, the numerical results of the three turbulence models are close or slightly lower than the experimental values, which are in good agreement. Under the wind direction angle of 0°, there is only one windward surface. Under the wind field of class D, the numerical results of the WALE model at the maximum wind pressure are 2.28% lower than those of TJ-2 test, and the results of SM and DSM are 0.24% higher than those of TJ-2,

respectively. Under class B wind field, the results of the WALE model at the maximum wind pressure are 5.38% lower than TJ-2, SM is 2.65% lower than TJ-2, and DSM is 6.77% lower than TJ-2. There are two windward surfaces at 45° wind direction angle. The numerical results of the three turbulence models are in good agreement with the test results of NPL and TJ-2, the test results of TJ-2 are more consistent with the long windward surface of the building, and the test results of NPL are more consistent with the short windward surface of the building.

The results of the three turbulence models are different from the experimental results for the positions belonging to the gas separation zone, such as the side and leeward surface. Under the wind direction angle of 0°, under the wind fields of D and B, the numerical results of the three turbulence models on the side are closer to the TJ-2 test results and between the two test results on the leeward side. The change
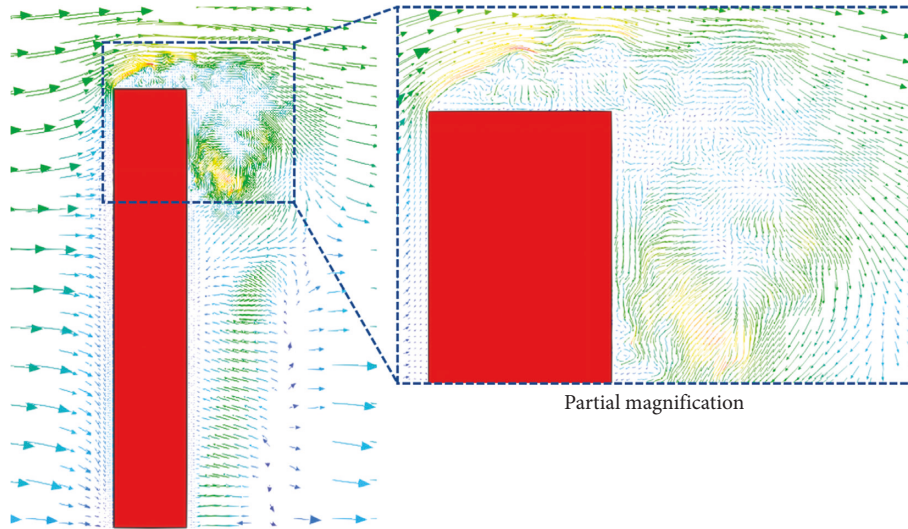
FIGURE 8: Velocity distribution of the wale model of class D wind farm passing through the center line of building.

law of the test results on the leeward side is more stable, while the change law of the numerical results of the three turbulence models on the leeward side is more intense. The reason is that the LES method can catch some low-frequency pulsating components missing in the test incoming flow due to the limitation of laboratory cross section, so the test results are different from the numerical results. Comparing the simulation results of turbulence models on the side and leeward side under class B wind field with the TJ-2 test results, the maximum error of the WALE model is 21.7%, SM is 28.1%, and DSM is 24.4%.

Combined with the numerical results of the average wind pressure coefficient on the leeward side under the wind direction angle of 45°, the simulation results of each turbulence model are between TJ-2 and NPL test results under class D wind field. Comparing the simulation results of various turbulence models on the leeward side under class B wind field with the TJ-2 test results, the maximum error of the WALE model is 19.7%, the maximum error of SM is 17.6%, and the maximum error of DSM is 16.1%.

On the whole, there is little difference among the simulation results of the three turbulence models. The windward side is under positive pressure, and all bear negative pressure on the crosswind side and leeward side. The numerical simulation results are between the NPL and TJ-2 test results. The WALE model has the highest accuracy, and the overall trend is the closest to the test results; DSM has less error and more stable value than SM. The errors of the three turbulence models are less than 30%, which meets the requirements of engineering application.

4.2. Isoline of Wind Pressure Coefficient. The wind pressure coefficient contours CP of the windward, side, leeward, and top surfaces of the three turbulence calculation models are shown in Figure 6. Taking the numerical simulation results under class D wind field with 0° wind direction angle as an example, the differences between the three turbulence models are compared.

Under the action of frontal incoming wind, the windward side is under positive pressure, and the other sides are under negative pressure. The positive pressure borne by the CAARC standard mould is the largest in the middle of the windward surface and decreases to both sides and downward, and the bottom is the smallest. This is because the wind speed in the wind field increases exponentially with the height, so the wind pressure coefficient of the upper part of the building is larger than that of the lower part. The leeward side of the building bears negative pressure (suction), and the suction presents the law of large in the upper part, small in the lower part, slightly large on both sides, and small in the middle. The air flow on the side and top of the building is in the separation zone, and the test results of each turbulence calculation model domain are different, but they all meet the test requirements. In general, the three turbulence models are closer to the NPL test results.

When the incoming flow is at 0° and 45° wind direction angles, the velocity distribution of 2/3H height horizontal plane after the air flow is blocked and is shown in Figures 7(a) and 7(b), respectively. In both cases, two large vortices were generated on the leeward side. This causes suction. Figure 8 shows the vector diagram of wind speed passing through the center line of the building. Take the calculation results of the wale model of class D wind field as an example.

When the fluid flows through the flow surface of the building, the boundary layer separation occurs. In the positive pressure zone, the inertial force and pressure difference of the fluid overcome the viscous force of the fluid and make the fluid flow smoothly downstream along the solid wall. In the negative pressure area, the inertial force of the fluid should not only overcome the viscous force, but also overcome the reverse pressure generated by the strong negative pressure. Under certain conditions, the fluid particles near the solid wall will stagnate or even move upstream; that is, eddy current will be formed. The boundary layer separation will form a separation zone and wake at the rear of the building.

As can be seen from Figure 8, at about 2/3 of the height, the air flow has a frontal stagnation point, and the velocity direction of this point is perpendicular to the positive windward surface. Above this point, the flow rises and crosses the top surface of the building. Below this point, the air flows downward and flows to the ground, and the air on the windward side rolls downward. Therefore, a horizontal rolling is formed on the windward side of the building close to the ground, forming a standing vortex area. The distribution of wind pressure coefficient is shown in Figure 6(a). On the leeward side, a large vortex and some small vortices are formed along the height direction of the building. The distribution of wind pressure coefficient is shown in Figure 6(c). A certain vortex is also generated at the corner of the building roof, which causes suction. Generally speaking, the air flow has a downward trend towards the windward side and flows around both sides and the top surface. At the same time, it can be seen from the velocity diagram that the flow structure around the square column is highly complex, full of collision, separation, vortex, surround, and reflux. The vortex is rolled down around the velocity line above the square column, and the velocity line at the bottom is rolled up. The vortices are intertwined and flow downward. Therefore, the downstream flow field of the square column is highly vortex and disorder, which is one of the reasons for the low accuracy of numerical simulation in the separation zone of the square column.

5. Conclusions

Three turbulence models are constructed based on three large eddy simulation (LES) methods, namely, MRT-LBM-WALE, MRT-LBM-DSM, and MRT-LBM-SM. The CAARC standard high-rise buildings are numerically simulated, respectively, and the numerical results are compared with the test results of TJ-2 of Tongji University and NPL National Physical Laboratory. The following conclusions can be drawn:

(1) The flow around a bluff body in the atmospheric boundary layer is very complex. It is full of phenomena such as collision, separation, vortex, encirclement, and backflow. The stress characteristics of the building wall can only be measured by a test, while the numerical simulation can better reflect the flow characteristics of the wind environment around the high-rise building and the distribution of surface wind pressure.

(2) On the windward side, the wind pressure coefficient of the numerical simulation results is in good agreement with the experimental results, and there is positive pressure on the windward side. It is the largest in the middle of the windward side and minimum on both sides and below. The leeward side of the building bears negative pressure (suction). Generally, the negative pressure on both sides is slightly larger, the middle is small, and the negative pressure distribution on the whole back is relatively uniform. The side of the building bears suction, and

the test value is greater than the calculated value. The results of the three turbulence models are different from the experimental results, but the maximum error is also within 30%. This indicates that the numerical simulation based on the MRT-LBM-LES model can meet the accuracy of engineering application.

(3) The numerical simulation based on the MRT-LBM-LES model can better simulate the smaller turbulence scale and more truly restore the turbulence characteristics around the building in practice.

Data Availability

The data used to support the findings of the study are included within the article.

Conflicts of Interest

The authors declare no conflicts of interest.

Acknowledgments

References

[1] X. Dong, J. H. Ye, Y. F. Zhou, and T. Zuo, "Wind-induced effects and leeward flow patterns of a CAARC standard tall building model," *Journal of Vibration and Shock*, vol. 38, no. 24, pp. 122–130, 2019.

[2] Y. Li and Q. S. Li, "Wind tunnel test research on caarc standard tall building model," *Industrial Construction*, vol. 43, no. S1, pp. 222–226, 2013.

[3] B. Msta, B. Jcb, B. Sc, and A. HHHK, "Towards a standard cfd setup for wind load assessment of high-rise buildings: Part 1-benchmark of the caarc building," *Journal of Wind Engineering and Industrial Aerodynamics*, vol. 33, no. 2, 2020.

[4] S. L. Li, L. L. Liu, H. Wu, and N. S. Y. P. Jiang, "New test method of wind pressure coefficient based on CAARC standard model determined using vehicle driving wind," *Experimental Techniques*, vol. 43, no. 6, pp. 707–717, 2019.

[5] F.-Q. Meng, B.-J. He, J. Zhu, and D.-X. A. Z.-Q. Zhao, "Sensitivity analysis of wind pressure coefficients on CAARC standard tall buildings in CFD simulations," *Journal of Building Engineering*, vol. 16, pp. 146–158, 2018.

[6] T. Okaze, H. Kikumoto, H. Ono, and M. N. T. K. T. Y. K. R. Y. Imano, "Large-eddy simulation of flow around an isolated building: a step-by-step analysis of influencing factors on turbulent statistics," *Building and Environment*, vol. 202, Article ID 108021, 1 page, 2021.

[7] S. H. Huang, Q. S. Li, and S. L. Xu, "Numerical evaluation of the effect of wind loads on high-rise steel buildings based on computational fluid dynamics," *Steel Construction*, vol. 2, no. 1, 82 pages, 2008.

[8] A. L. Braun and A. M. Awruch, "Aerodynamic and aeroelastic analyses on the CAARC standard tall building model using numerical simulation," *Computers & Structures*, vol. 87, no. 9-10, pp. 564–581, 2009.

[9] S. J. Daniels, I. P. Castro, and Z.-T. Xie, "Peak loading and surface pressure fluctuations of a tall model building," *Journal of Wind Engineering and Industrial Aerodynamics*, vol. 120, pp. 19–28, 2013.

[10] A. Elshaer, H. Aboshosha, G. Bitsuamlak, and A. El Damatty, "LES evaluation of wind-induced responses for an isolated and a surrounded tall building," *Engineering Structures*, vol. 115, pp. 179–195, 2016.

[11] S. F. Nie, X. H. Zhou, T. H. Zhou, and Y. Shi, "Numerical simulation of 3D atmospheric flow around a bluff body of CAARC standard high-rise building model," *Journal of Civil , Architectural & Environmental Engineering*, vol. 31, no. 06, pp. 40–46, 2009.

[12] Q. Zhou, H. Liao, and S. Cao, "Numerical study of flow characteristics around square cylinder at high Reynolds number," *Journal of Southwest Jiaotong University*, vol. 53, no. 3, pp. 533–539, 2018.

[13] W. Li, H. W. Niu, X. G. Hua, and Z. Q. Chen, "Large eddy simulation of measured turbulent wind field on long-span bridges," *China Journal of Highway and Transport*, vol. 11, pp. 1–18, 2022.

[14] C. Liu, J. F. Huang, and C. Shao, "Research on wake structure of three-dimensional tandem multi-cylinder flow based on LBM-LES," *Chinese Journal of Applied Mechanics*, vol. 39, no. 1, pp. 186–194, 2022.

[15] Q. L. Zhang and H. F. Jing, "Study on the flow pattern in three-dimensional lid-driven cavities with curved boundary based on MRT-LBM," *Chinese Journal of Computational Physics*, vol. O4, pp. 1–14, 2021.

[16] Y. Luo, H. Liu, H. Xue, and K. Lin, "Large-eddy simulation evaluation of wind loads on a high-rise building based on the multiscale synthetic eddy method," *Advances in Structural Engineering*, vol. 22, no. 4, pp. 997–1006, 2019.

[17] H. Yu, L.-S. Luo, and S. S. Girimaji, "LES of turbulent square jet flow using an MRT lattice Boltzmann model," *Computers & Fluids*, vol. 35, no. 8-9, pp. 957–965, 2006.

[18] G. Eitel-Amor, M. Meinke, and W. Schröder, "A lattice-Boltzmann method with hierarchically refined meshes," *Computers & Fluids*, vol. 75, pp. 127–139, 2013.

[19] D. K. Lilly, "A proposed modification of the Germano sub-grid-scale closure method," *Physics of Fluids A: Fluid Dynamics*, vol. 4, no. 3, pp. 633–635, 1992.

[20] M. Germano, U. Piomelli, P. Moin, and W. H. Cabot, "A dynamic subgrid-scale eddy viscosity model," *Physics of Fluids A: Fluid Dynamics*, vol. 3, no. 7, pp. 1760–1765, 1991.

[21] D. Teso-Fz-Betoo, M. Juica, K. Portal-Porras, U. Fernandez-Gamiz, and E. Zulueta, "Estimating the reattachment length by realizing a comparison between URANS k-omega SST and LES WALE models on a symmetric geometry," *Symmetry*, vol. 13, no. 9, pp. 160–165, 2021.

[22] Z. B. Zhou, Q. H. Zhang, and J. F. Zhang, "Three-dimensional lattice Boltzmann simulation of oscillatory boundary layer flow over rippled bed," *Journal of Tianjin University*, vol. 52, no. 04, pp. 430–439, 2019.

[23] M. Weickert, G. Teike, O. Schmidt, and M. Sommerfeld, "Investigation of the LES WALE turbulence model within the lattice Boltzmann framework," *Computers & Mathematics with Applications*, vol. 59, no. 7, pp. 2200–2214, 2010.

[24] J. Lei, C. Xu, F. F. Xue, H. P. Pan, C. Chen, and H. Yi, "Study on aerodynamic field of steep hill wind farm by different models of LES," *Water Resources and Power*, vol. 36, no. 1, pp. 203–207, 2018.

[25] Y. Luo, H. Liu, Q. Huang, and H. K. Xue, "A multi-scale synthetic eddy method for generating inflow data for LES," *Computers & Fluids*, vol. 156, pp. 103–112, 2017.

[26] C. T. Jiang, H. Zhou, M. M. Xia, J. X. Tang, and Y. Wang, "Viscous absorbing boundary of the multiple-relaxation-time lattice Boltzmann method," *Oil Geophysical Prospecting*, vol. 56, no. 05, pp. 1030–1038, 2021.

[27] Y. P. Qu, K. Zhang, and S. Y. Chen, "Research on three-block local grid refinement method in MRT-LBM," *Transactions of Beijing Institute of Technology*, vol. 38, no. 05, pp. 441–448, 2018.

[28] B. Lin, X. Y. Sun, Y. Wu, and S. Z. Shen, "Windtunnel test and CFD numerical simulation of wind-induced loads on gy mnasium roof of daqing petroleuminstitute," *Journal of Shenyang Jianzhu University Natural Science*, vol. 22, no. 03, pp. 357–361, 2006.

[29] H. M. Wang, X. G. Wang, and S. Y. Wang, "Study of wind load distribution in special-shaped buildings under typical strong wind," *Journal of Henan University of Science And Technology: Natural Science*, vol. 43, no. 01, pp. 57–63, 2022.

[30] J. Wang, W. Zhang, and M. Fečkan, "Periodic boundary value problem for second-order differential equations from geo-physical fluid flows," *Monatshefte für Mathematik*, vol. 195, no. 3, pp. 523–540, 2021.

[31] T. Cebeci, K. C. Chang, C. Li, and J. H. Whitelaw, "Turbulence models for wall boundary layers," *AIAA Journal*, vol. 24, no. 3, pp. 359-360, 1986.

[32] H. Wu, G.-Y. Zhao, and S.-W. Ma, "Failure behavior of horseshoe-shaped tunnel in hard rock under high stress: phenomenon and mechanisms," *Transactions of Nonferrous Metals Society of China*, vol. 32, no. 2, pp. 639–656, 2022.

[33] G. S. Han, Y. Zhou, R. C. Liu, Q. Tang, X. Wang, and L. Song, "Infuence of surface roughness on shear behaviors of rock joints under constant normal load and stifness boundary conditions," *Natural Hazards*, vol. 2, no. 2, pp. 1–15, 2022.

[34] X. Li, Z. Cao, and Y. Xu, "Characteristics and trends of coal mine safety development," *Energy Sources, Part A: Recovery, Utilization, and Environmental Effects*, vol. 2, no. 2, pp. 1–19, 2020.

[35] S. Liu, X. Li, D. Wang, and D. Zhang, "Investigations on the mechanism of the microstructural evolution of different coal ranks under liquid nitrogen cold soaking," *Energy Sources, Part A: Recovery, Utilization, and Environmental Effects*, vol. 1, no. 1, pp. 1–17, 2020.

[36] L. Xl, C. Sj, Z. Qm, G. Xin, and F. Fan, "Research on theory, simulation and measurement of stress behavior under regenerated roof condition," *Geomechanics and Engineering*, vol. 26, no. 1, pp. 49–61, 2021.

[37] X. l. Li, S. J. Chen, S. M. Liu, and Z. H. Li, "AE waveform characteristics of rock mass under uniaxial loading based on Hilbert-Huang transform," *Journal of Central South University*, vol. 28, no. 6, pp. 1843–1856, 2021.

[38] X. Li, S. Chen, and S. M. H. Wang, "Study on in situ stress distribution law of the deep mine: taking linyi mining area as an example," *Advances in Materials Science and Engineering*, vol. 2021, no. 4, pp. 1–11, 2021.

[39] W. Shen, G. Shi, Y. Wang, and J. R. X. Bai, "Tomography of the dynamic stress coefficient for stress wave prediction in sedimentary rock layer under the mining additional stress," *International Journal of Mining Science and Technology*, vol. 31, no. 4, pp. 653–663, 2021.

[40] X. Kong, D. He, X. Liu et al., "Strain characteristics and energy dissipation laws of gas-bearing coal during impact fracture process," *Energy*, vol. 2, no. 42, pp. 12–28, 2022.

[41] X. Kong, S. Li, E. Wang, and X. Y. P. H. S. Z. Wang, "Experimental and numerical investigations on dynamic mechanical responses and failure process of gas-bearing coal under impact load," *Soil Dynamics and Earthquake Engineering*, vol. 142, Article ID 106579, 2021.

[42] Z. Li, X. Zhang, and Y. M. Wei, "Experimental study of electric potential response characteristics of different lithological samples subject to uniaxial loading," *Rock Mechanics and Rock Engineering*, vol. 54, no. 1, pp. 397–408, 2021.

[43] Y. Niu, E. Wang, Z. Li et al., "Identification of coal and gas outburst-hazardous zones by electric potential inversion during mining process in deep coal seam," *Rock Mechanics and Rock Engineering*, vol. 3, 2022.

[44] W. Zhong, J. O. Yang, D. Yang, X. J. Wang, Z. Q. Guo, and K. J. Hu, "Effect of the in situ leaching solution of ion-absorbed rare earth on the mechanical behavior of basement rock," *Journal of Rock Mechanics and Geotechnical Engineering*, vol. 18, 2022.